



# Plasmon enhancement on photocatalytic hydrogen production over the Z-scheme photosynthetic heterojunction system

Hongqing Gao <sup>a,b</sup>, Peng Zhang <sup>a,b,\*</sup>, Jiangtao Zhao <sup>a,b</sup>, Yongshang Zhang <sup>a,b</sup>, Junhua Hu <sup>a,b,\*\*</sup>, Guosheng Shao <sup>a,b,c</sup>

<sup>a</sup> School of Materials Science and Engineering, Zhengzhou University, Zhengzhou 450001, People's Republic of China

<sup>b</sup> State Centre for International Cooperation on Designer Low-carbon and Environmental Materials (SCICDLCEM), Zhengzhou University, Zhengzhou 450001, Henan, People's Republic of China

<sup>c</sup> Institute for Renewable Energy and Environmental Technologies, University of Bolton, Bolton BL35AB, UK



## ARTICLE INFO

### Article history:

Received 26 November 2016

Received in revised form 9 March 2017

Accepted 20 March 2017

Available online 22 March 2017

### Keywords:

Electrospinning

Z-scheme

Photocatalysis

Hydrogen production

Synergistic effect

## ABSTRACT

Direct evidence of plasmon for enhanced H<sub>2</sub> production is observed in photocatalytic water reduction by using TiO<sub>2</sub>/WO<sub>3</sub> electrospun nanofibers decorated with Au nanoparticles. The H<sub>2</sub> production rate of the as-prepared composite nanofibers was greatly enhanced compared with pure TiO<sub>2</sub> nanofibers (S0) and TiO<sub>2</sub>/WO<sub>3</sub> nanofibers (S1). The enhanced activities were mainly attributed to the Schottky effect and Z-scheme photosynthetic heterojunction system, in this system, WO<sub>3</sub> as a hole collector and Au as an electron collector, promoting effective charge separation. More importantly, Surface Plasmon Resonance (SPR) effect of Au further promoted charge separation and absorption of visible light. On the basis of the Z-scheme photosynthetic heterojunction system, the synergistic effect of Schottky and SPR effect further improve the performance of photocatalytic H<sub>2</sub> production, which were directly evidenced by photocurrent, electrochemical impedance spectroscopy (EIS) and ultraviolet Photoelectron Spectrometer (UPS) analysis. Besides, the synthesis route delivered three-dimensional sheets on the basis of interwoven nanofibrous networks, which can be readily recycled for the circular application of a potent photocatalyst system.

© 2017 Elsevier B.V. All rights reserved.

## 1. Introduction

A promising technique of hydrogen production from solar energy by use of semiconductor photocatalysis has attracted much attention since its discovery by Honda-Fujishima [1]. TiO<sub>2</sub> has been extensively used as an efficient photocatalyst for water splitting because of its high photoactivity and chemical inertness [2,3]. However, the low charge-separation efficiency of photogenerated electron-hole pairs and poor visible-light absorption still severely constrain their further development especially toward commercial production [4–6]. In view of these scientific problems, research found that the construction of heterostructures is an effective method to reduce the recombination of photoinduced electron-hole pairs [7–9]. Therefore, a large number of Z-scheme heterojunction photosynthetic systems such as CdS-WO<sub>3</sub>, TiO<sub>2</sub>-Si, TiO<sub>2</sub>-C<sub>3</sub>N<sub>4</sub> and ZnO-C<sub>3</sub>N<sub>4</sub> have been investigated and used for photocatalytic reactions [10–13]. Previous research and our work

found that the CB of WO<sub>3</sub> is between the CB and VB of TiO<sub>2</sub>, and the VB of WO<sub>3</sub> is lower than the VB of TiO<sub>2</sub>, thus coupling WO<sub>3</sub> with TiO<sub>2</sub> can form an artificial Z-scheme photocatalytic system, which can promote the separation of photogenerated electron-hole pairs by transferred electrons of WO<sub>3</sub> to the VB of TiO<sub>2</sub> [14]. On the other hand, how to further enhance the separation rates of photogenerated electron-hole pairs and improve the quantum yield is another challenge to improve the photocatalytic activities. It has been demonstrated successfully by different groups including ours that the construction of heterojunctions of metal nanoparticles (e.g. Au, Ag and Pt) and TiO<sub>2</sub> is a good method [15–17]. Among these metals, Au is a popular choice because of its high chemical stability and its ability to generate surface plasmons at the desired wavelength [18–21]. However, many researchers focus on designing novel material in which insulating layer was introduced to blocking the electron transfer between metal and semiconductor rather than research the coexistence of Schottky and Surface Plasmon Resonance (SPR) effects [22]. So it's of great significance to construct the Z-scheme heterojunction system with Au nanoparticle, and investigative the impact of the coexistence of the Schottky and SPR effects with the Z-scheme heterojunction for the photocatalytic hydrogen production performance.

\* Corresponding author. Tel.: +86 37167739798.

\*\* Corresponding author.

E-mail addresses: [Zhangp@zzu.edu.cn](mailto:Zhangp@zzu.edu.cn) (P. Zhang), [Hujh@zzu.edu.cn](mailto:Hujh@zzu.edu.cn) (J. Hu).

In this paper, we provided an effective route to synthesize ternary Z-scheme  $\text{TiO}_2/\text{WO}_3/\text{Au}$  heterostructures composite nanofibers by a facile electrospinning technique and subsequent annealing in air. The amount of Au nanoparticles can be regulated by varying the dosage of chloroauric acid in the precursor solution. The investigation of photocatalytic ability indicated that the as-prepared samples exhibited enhanced photocatalytic  $\text{H}_2$  production rates under sun-light irradiation, the enhanced activities were mainly attributed to the Schottky effect and Z-scheme photosynthetic heterojunction system,  $\text{WO}_3$  as a hole collector and Au as an electron collector, promoting effective charge separation. More importantly, SPR effect of Au further promoted charge separation and absorption of visible light. On the basis of the Z-scheme heterojunction system, the synergistic effect of Schottky and SPR effect further improve the performance of photocatalytic  $\text{H}_2$  production. Besides, the electrospun three-dimensional nanofibrous networks can be well recycled for the photocatalyst system [23,24].

## 2. Experimental section

### 2.1. Preparation of the ternary Z-scheme $\text{TiO}_2/\text{WO}_3/\text{Au}$ heterostructures composite nanofibers

The ternary Z-scheme  $\text{TiO}_2/\text{WO}_3/\text{Au}$  heterostructures composite nanofibers were prepared by electrospinning technique. Typically, 2 g tetrabutyl titanate (TBT) (Aladdin, CP, 98.0%), 0.15 g ammonium tungstate (Aldrich, 99.95%) (Our previous study showed a higher photocatalytic activity in this proportion), different amount of  $\text{HAuCl}_4$  absolute alcohol solution were dissolved in a mixture containing 10 ml ethanol (Sinopharm Chemical Reagent, 99.7%) and 6 ml acetic acid (Sinopharm Chemical Reagent, 99.5%), after magnetic stirring for 20 min, 1.1 g Polyvinyl Pyrrolidone (PVP,  $M_w = 1,300,000$ ) were added into the solution slowly under vigorous stirring, the resulting solution was magnetic stirred for 12 h at room temperature. The mass concentration of  $\text{HAuCl}_4$  ranged from 0.3% (S2) to 0.45% (S3). Subsequently, the above precursor solutions were drawn into a hypodermic syringe. The positive terminal of a variable high voltage power supply was connected to the needle tip of the syringe while the other terminal was connected to the collector. The distance between the needle tip and collector was  $\sim 15$  cm, and the voltage was set at 15 kV. The as-collected nanofibers were calcined at  $520^\circ\text{C}$  for 30 min to form ternary Z-scheme  $\text{TiO}_2/\text{WO}_3/\text{Au}$  heterostructures composite nanofibers. We also use the same method prepare  $\text{TiO}_2$  (S0) nanofibers and  $\text{TiO}_2/\text{WO}_3$  nanofibers (S1) as a contrast.

### 2.2. Characterization

The morphology of the as-prepared nanofibers was observed by field emission scanning electron microscopy (FESEM, JSM-7500F) and transmission electron microscope (TEM, FEI Tecnai G2 F20). The crystallization and the phase transition were studied by XRD (Rigaku Ultima IV) with  $\text{Cu K}\alpha$  radiation (wavelength = 0.15406 nm) from  $20^\circ$  to  $80^\circ$ , at a scanning rate of  $4^\circ/\text{min}$ . The diffuse reflectance spectra of all samples were recorded on a UV/Vis spectrophotometer (Shimadzu, model UV 3600) equipped with an integrating sphere in the range of 300–800 nm and standard  $\text{BaSO}_4$  powder was used as a reference. The X-ray photoelectron spectroscopy (XPS) and Photoelectron Spectrometer (UPS) were measured by the multifunctional X-ray photoelectron spectroscopy (AXIS Ultra<sup>DLD</sup>, Kratos Analytical Inc).

### 2.3. Photoelectrochemical experiment

Photoelectrochemical measurements were carried out in a quartz cubic urn with a conventional three-electrode process on

an electrochemical workstation (AMETEK, PARSTAT 4000, America). The as-synthetic photoanode was the working electrode, and a Pt wire and  $\text{Ag}/\text{AgCl}$  electrode served as the counter electrode and reference electrode, respectively. The electrolyte was a 0.2 M  $\text{Na}_2\text{SO}_4$  aqueous solution. The photoanode surface has an illuminated area of  $1.5 \times 1.5 \text{ cm}^2$ . All the samples (0.1 g) mixing with polyethylene glycol (0.05 g) and water (0.35 ml) were deposited on the FTO conducting glass, with thin transparent cover glass to seal avoiding samples fall off. The light source was a 300 W Xe lamp (Beijing Perfectlight Co. Ltd, PLS-SXE-300). The photocurrent response spectroscopy was carried out at a constant potential of +0.9 V to the working photoanode. Electrochemical impedance spectra (EIS) were measured at an open-circuit voltage. A sinusoidal ac perturbation of 5 mV was applied to the electrode over the frequency range of 100 mHz to 10 kHz. The incident photon-to-current conversion efficiency (IPCE) of the samples was tested using a power source (Newport 300 W Xenon lamp, 66920) with a monochromator (Newport Cornerstone 260) and a multimeter (Keithley 2001). In our work, the IPCE spectrum was conducted as a function of wavelength from 350 to 800 nm by using the as-synthetic photoanode as working electrode and a Pt wire as the counter electrode. All measurements were carried out at room temperature.

### 2.4. Photocatalytic hydrogen production evaluation

Photocatalytic hydrogen production was proceed on an equipment of online analysis system (LabSolar-III AG, Beijing Perfectlight Co. Ltd.) directly connected with gas chromatography (GC-7860). A 300W Xe arc lamp (PLS-SXE 300, Beijing Perfectlight Co. Ltd) was used as the light source, the light intensity of UV, Vis and  $\text{UV} + \text{vis}$  is  $2.2 \text{ mW/cm}^2$ ,  $9.6 \text{ mW/cm}^2$  and  $10.1 \text{ mW/cm}^2$ . 0.05 g as-prepared sample was mixed with 45 ml deionized water and 25 ml methyl alcohol (anhydrous, Sinopharm Chemical Reagent, 99.5%) under strong magnetic stirring for sufficient mixing. The advantage of online analysis system for hydrogen production is that we could test the amount of  $\text{H}_2$  by real-time monitoring and the generated gas was pumped to gas chromatography every 1 h to get the in situ average hydrogen production rate.

## 3. Results and discussion

### 3.1. SEM of the as-prepared ternary Z-scheme $\text{TiO}_2/\text{WO}_3/\text{Au}$ heterostructures composite nanofibers

The morphologies of the as-prepared ternary Z-scheme  $\text{TiO}_2/\text{WO}_3/\text{Au}$  heterostructures composite nanofibers were examined by scanning electron microscopy (SEM). It could be seen from Fig. 1A that the 3D web structure composed of uniform and straight nanofibers, and the length of these randomly oriented nanofibers could reach up to several micrometers or more. According to the enlarged image in Fig. 1B, the diameter of those nanofibers ranged from 300 to 350 nm. And, the enlarged fiber had a relatively smooth surface without secondary nanostructures. The elements mapping of as-prepared S2 sample in Fig. 1C–F show the distribution of the elements of Ti, O, W and Au, indicating a uniform distribution of the various elements in the sample, besides, the element of Au nanoparticle distributed in the surface and the interior of the nanofibers (Fig. S1).

### 3.2. TEM of the as-prepared ternary Z-scheme $\text{TiO}_2/\text{WO}_3/\text{Au}$ heterostructures composite nanofibers

In order to obtain more detailed information about the morphology and crystalline structure of the ternary Z-scheme  $\text{TiO}_2/\text{WO}_3/\text{Au}$  heterostructures composite nanofibers, the transmission electron microscopy (TEM) and high-resolution transmission electron

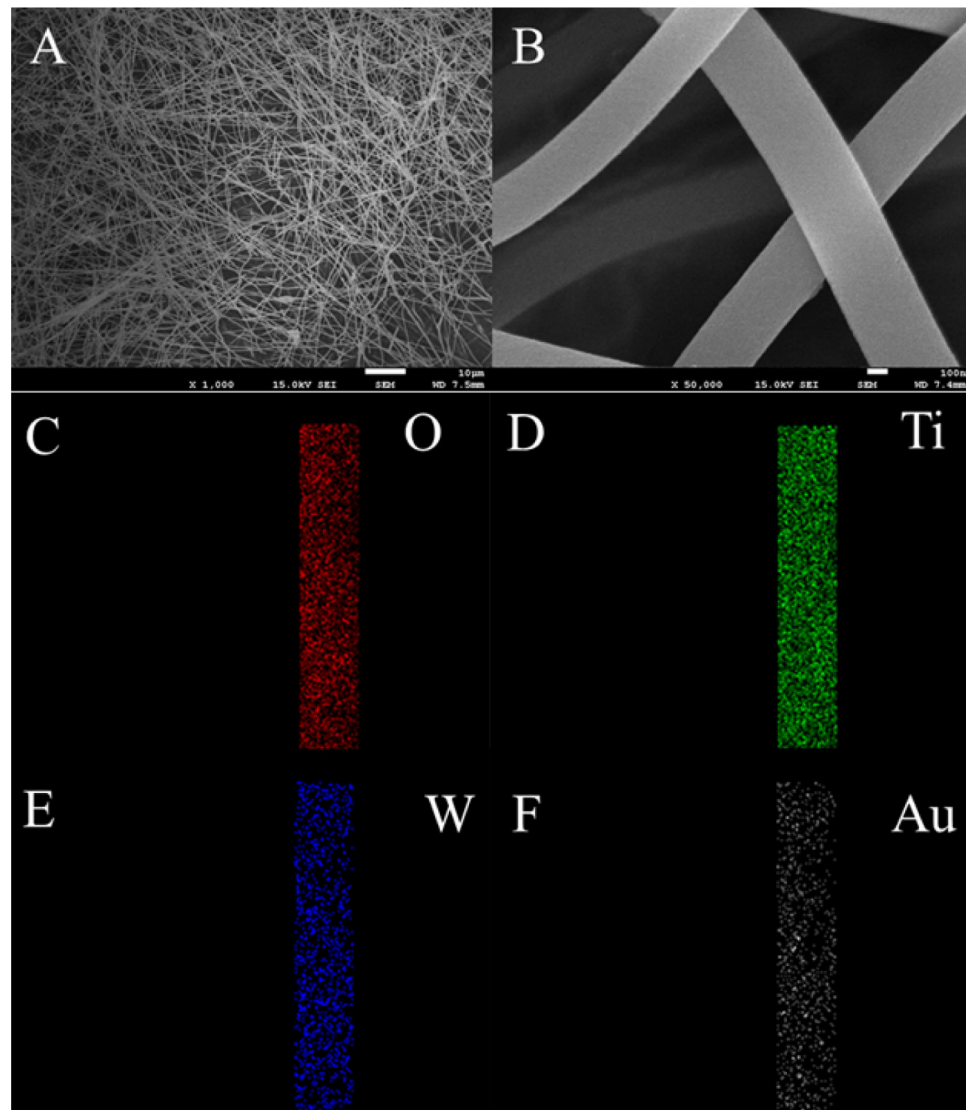


**Fig. 1.** (A), (B) SEM image of as-prepared S2 sample; (C)–(F) elements mapping of as-prepared S2 sample.

microscopy (HRTEM) observation were carried out. **Fig. 2A** showed the typical TEM of the ternary Z-scheme  $\text{TiO}_2/\text{WO}_3/\text{Au}$  heterostructures composite nanofibers. It can be observed that the composite nanofibers have a smooth surface, which is consistent with the result of the SEM image. A close investigation of S2 sample by high-resolution TEM (HRTEM) (**Fig. 2B–F**) reveals that Au nanoparticles with a diameter of  $\sim 5$  nm distributed in the fiber's interior and surface, this results indicate that Au and  $\text{TiO}_2$  nanoparticles have a good contract, which lead to the formation of close Schottky contact between Au and  $\text{TiO}_2$  nanoparticles. Besides, the interplanar spacing of  $0.352\text{ nm}$  and  $0.367\text{ nm}$  attribute to the (101) plane of anatase  $\text{TiO}_2$  and the (200) plane of  $\text{WO}_3$ , respectively.

### 3.3. X-ray diffraction (XRD) patterns

The crystallographic structure and phase purity of the as-prepared samples were identified by X-ray diffraction (XRD) patterns, as shown in **Fig. 3**. Five reflection peaks appeared at  $2\theta = 25.3^\circ$ ,  $37.7^\circ$ ,  $48^\circ$ ,  $53.8^\circ$ ,  $62.6^\circ$  are indexed to the (101), (004), (200), (105), (204), respectively. It displayed well-structured diffraction patterns for anatase  $\text{TiO}_2$  phase (ICSD: 01-070-7348), and it is in very good agreement with previous reports [25]. And the weak peaks at  $24.2^\circ$  and  $33.9^\circ$  can be indexed to the (200) and (220)

crystal planes of the anatase phase of  $\text{WO}_3$  (ICSD: 00-001-0486), the peaks of  $\text{WO}_3$  are very peak because of its low concentration. Besides, there are no Au peaks in the XRD patterns because of its small size and low concentration.

### 3.4. Characterization of the electronic structure of the as-prepared samples

The photocatalytic efficiency is highly related to the light absorption including amount, wavelength range, and absorption peak position. The UV-vis diffuse reflectance spectroscopy is an effective tool for light absorption measurement. **Fig. 4(A)** shows the UV-vis diffuse reflectance spectroscopy of the as-prepared samples. The diffuse reflectance spectrum of  $\text{TiO}_2$  nanofibers only exhibited the fundamental absorption band in the UV region, there is no more absorption in visible wavelengths, it is assigned to the intrinsic band gap absorption of anatase  $\text{TiO}_2$  ( $E_g: \sim 3.2\text{ eV}$ ) [26]. Different from pure  $\text{TiO}_2$  nanofibers, there was a certain redshift after coupling with  $\text{WO}_3$ , it may be due to the narrow band gap of  $\text{WO}_3$  and the formation of complex oxide by  $\text{TiO}_2$  and  $\text{WO}_3$ , which prompting the separation of photogenerated electron-hole pairs. And, all the ternary Z-scheme  $\text{TiO}_2/\text{WO}_3/\text{Au}$  heterostructures composite nanofibers present an obvious absorption band centered at

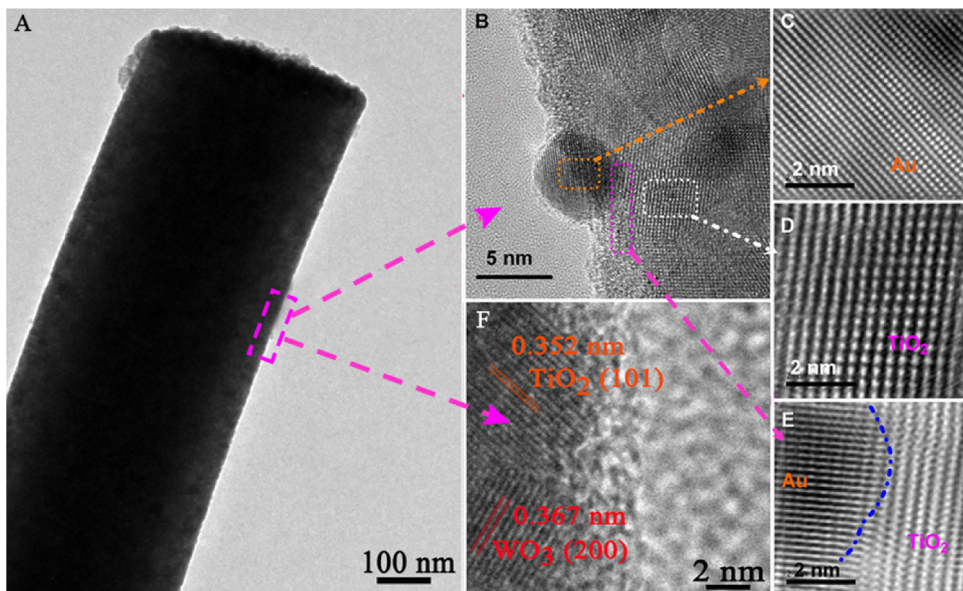


Fig. 2. TEM images of as-prepared S2 sample. (A) A low-resolution TEM image. (B–F) HRTEM images showing close contact and lattice correlations of as-prepared S2 sample.

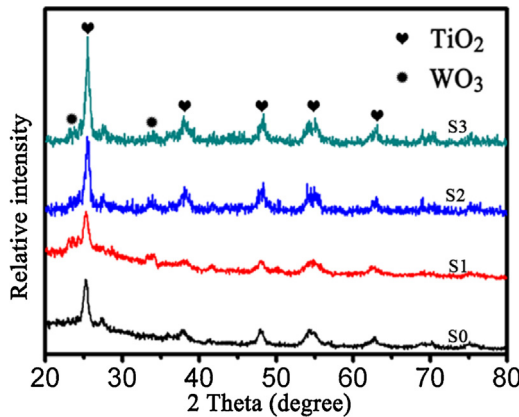
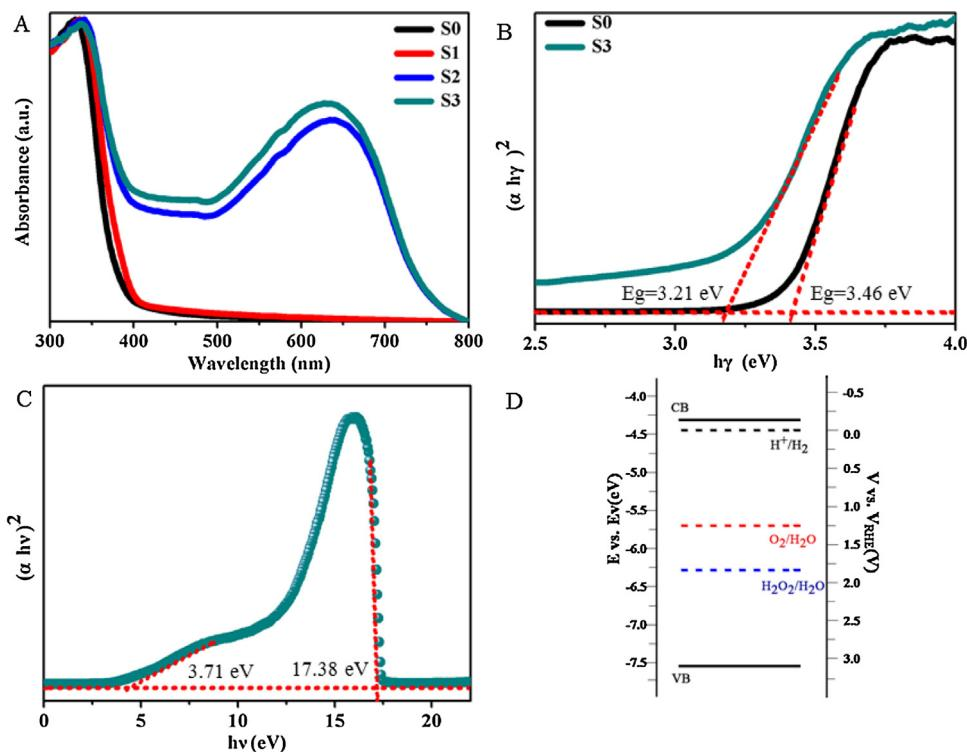


Fig. 3. XRD patterns of all the as-prepared samples.

~630 nm, which arises from the surface SPR effect of Au Nanoparticles [27]. The SPR position of Au is clearly red-shifted based on the special prepare methods, this similar phenomenon also founded in our previous work [28]. Besides, the Au SPR peak becomes more intensive with the increasing of the amount of Au nanoparticles. We plotted the image of  $(\alpha h\nu)^2$  and  $(h\nu)$  for the purpose of calculating the band gaps, as is shown in Fig. 4B, the Eg value of S0 and S3 are calculated to be 3.46 eV and 3.21 eV, respectively [29]. In order to further determine the ionization potential [equivalent to the valence band energy (Ev)] of S3 sample, we did the UPS experiment. As is shown in Fig. 4C, the Ev of S3 sample was calculated to be 7.53 eV by subtracting the width of the He I UPS spectra from the excitation energy (21.22 eV), thus the conduction band energy Ec of 4.32 eV can be calculated from Ev-Eg. According to the reference standard for which 0 eV versus reversible hydrogen electrode (RHE) equals  $-4.44$  eV versus evac (vacuum level) [30], the Eg, Ev, and Ec values of S3 sample are converted to electrochemical energy potentials in volts, Fig. 4D showed that the valence band of S3 sample is below the oxidation level for  $\text{H}_2\text{O}$  to  $\text{H}_2\text{O}_2$  or  $\text{O}_2$ , and the conduction band is above the reduction level for  $\text{H}_2$ , these results revealed the bands are properly for water splitting.

### 3.5. XPS spectra

In order to determine the existence of the various elements especially Au in the prepared sample and the valence, the chemical composition of the ternary Z-scheme  $\text{TiO}_2/\text{WO}_3/\text{Au}$  heterostructures composite nanofibers was studied by X-ray photoelectron spectroscopy (XPS) analysis. These results were observed in Fig. 5(A)–(E). The binding energy for C 1s peak at 283.4 eV was used as the reference for calibration. The survey spectrum as presented in Fig. 5A confirms that only Ti, W, Au, and O were present in the ternary Z-scheme  $\text{TiO}_2/\text{WO}_3/\text{Au}$  heterostructures composite nanofibers, which are in consistent with the EDS spectrum. High resolution XPS spectrum of Ti 2p, W 4f, Au 4f, and O 1s were observed in Fig. 5(B)–(E), respectively. The Ti 2p high resolution XPS spectra are analyzed in Fig. 5B. It could be seen from the spectrum that two peaks occurred at 457.6 and 463.3 eV were well corresponded with Ti 2p3/2 and Ti 2p 1/2 binding energies, respectively. The splitting of the 2p doublet was 5.7 eV, indicating a normal state of  $\text{Ti}^{4+}$  in the ternary Z-scheme  $\text{TiO}_2/\text{WO}_3/\text{Au}$  heterostructures composite nanofibers. Fig. 5C depicted the spin-orbit splitting of W 4f and can be deconvoluted into a doublet with binding energy peaks at 34.3 eV and 36.2 eV, resulting from the emission of W 4f 7/2 and W 4f 5/2 that might belong to the  $\text{W}^{6+}$  oxidation state of tungsten atoms and this is in good agreement with previously reported results. The Au 4f signals are shown in Fig. 5D, the presented Au 4f7/2 and Au 4f 5/2 peaks are located at 82.4 and 86.1 eV, respectively, which well agree with the values of the metallic  $\text{Au}^0$  state [31]. Fig. 5E shows the O 1s signal was well fitted with three contributions. The peak at binding energy of 528.4 eV was attributed to the O in  $\text{TiO}_2$  and  $\text{WO}_3$ , the peak at 528.9 and 529.3 eV should be ascribed to surface hydroxyl groups, and adsorbed  $\text{O}_2$  species, respectively. All of these XPS results and other characterizations gave the insight that the ternary Z-scheme  $\text{TiO}_2/\text{WO}_3/\text{Au}$  heterostructures composite nanofibers were composed of  $\text{TiO}_2$ ,  $\text{WO}_3$  and Au. Table S1 in the supporting information showed the experimental details and element contents of Au determined by XPS. We can determine the proportion of Au in the surface and in the internal in the fibers by the amount of Au added in the precursor solution, and better research the effect of Au in different position. Besides, the result showed that the content of Au increased



**Fig. 4.** Characterization of the electronic structure of the as-prepared samples. (A) UV-vis absorption spectra of the as-prepared samples. (B)  $(\alpha h\nu)^2$  versus  $h\nu$  of S0 and S3 sample. (C) UPS spectra of S3 sample. (D) Band structure diagram for S3 sample.

with the addition of chloroauric acid, which is consistent with the theoretical results.

### 3.6. Photoelectrochemical test

The photocatalytic activities of the as-prepared samples were estimated by detecting the photocurrents generated. Photocurrents which were measured with 0.2 M  $\text{Na}_2\text{SO}_4$  solution as electrolyte gives an apparent response to light on/off for  $\text{TiO}_2$  nanofibers,  $\text{TiO}_2/\text{WO}_3$  nanofibers and the ternary Z-scheme  $\text{TiO}_2/\text{WO}_3/\text{Au}$  heterostructures composite nanofibers electrodes under the irradiation of UV+vis light, as shown in Fig. 6A. It was clear that fast and uniform photocurrent responses were observed in both electrodes and the photoresponsive phenomenon was entirely reversible. Under the irradiation of UV+vis light, the order of photocurrent is:  $\text{S0} < \text{S1} < \text{S2} < \text{S3}$ , indicating that our design idea is feasible. Such obviously differences between these photoelectrode probably owing to the nice light absorbance, the efficient electron transfer and the charge separation in the composites.

Such obviously different electrical conductivity between the  $\text{TiO}_2$  nanofibers,  $\text{TiO}_2/\text{WO}_3$  nanofibers and the ternary Z-scheme  $\text{TiO}_2/\text{WO}_3/\text{Au}$  heterostructures composite nanofibers can be confirmed by the electrochemical impedance spectroscopy (EIS). Fig. 6B displayed the EIS of those four electrodes. All the Nyquist plots impedance spectra were in open-circuit potential conditions and showed similar. The nonlinear regression fitting using a conventional Randle's circuit ( $R$  (QR)) routine [32] gave active charge transfer resistance for:  $\text{S3} < \text{S2} < \text{S1} < \text{S0}$ , which indicated that the structure of the ternary Z-scheme  $\text{TiO}_2/\text{WO}_3/\text{Au}$  heterostructures composite nanofibers could reduce the mass-transfer resistance and enhance the electrolyte penetration as well as ion diffusion in the host material because of the introduction of Au excellent electron-transporting and electron-accepting properties. Since a lower charge transfer resistance was indicative of recombination suppression by improved charge transport to the electrolyte, these

**Table 1**  
IPCE data in specific wavelength range.

Nanocatalysts	IPCE Enhanced Factor		
	360 nm	420 nm	630 nm
S0	5.45	0.32	0.045
S1	5.69	0.41	0.1
S3	6.59	0.92	0.56

results suggested that both  $\text{WO}_3$  and Au played important roles in improving the charge separation efficiency.

What's more, in order to further investigative the photoelectrochemical properties of as-prepared samples, we conducted IPCE testing of S0, S1, and S3 samples, as is shown in Fig. 7. And quantified its values at particular wavelength, shown in Table S2. From Fig. 7 and Table 1, we can see that the IPCE enhancement factor of S0, S1 and S3 sample in UV is 5.45, 5.69 and 6.59, compared to S0 sample, the IPCE values of S1 and S3 sample at 360 nm were increased 4.4% and 20.9% respectively. The IPCE enhancement factor of S0, S1 and S3 sample at 420 nm is 0.32, 0.41 and 0.92, indicating that there is a certain red shift after complexed with  $\text{WO}_3$  and Au. What's more, the IPCE enhancement factor of S0, S1 and S3 sample at 630 nm is 0.045, 0.1 and 0.56, respectively. These results showed that the higher IPCE values of S3 sample electrode were increased in not only UV region but also visible region, which can be attributed to the synergistic effect of SPR and Schottky effect of Au, and this is consistent with the results of the UV-vis diffuse reflectance spectra.

### 3.7. Photocatalytic hydrogen production activity

In order to determine the photocatalytic activity of these as-prepared samples, we utilized them for photocatalytic hydrogen production [33–35]. Photocatalytic hydrogen production of as-prepared samples was evaluated under 300W Xenon lamp irradiation using methanol as a scavenger. As is shown in Fig. 8A,

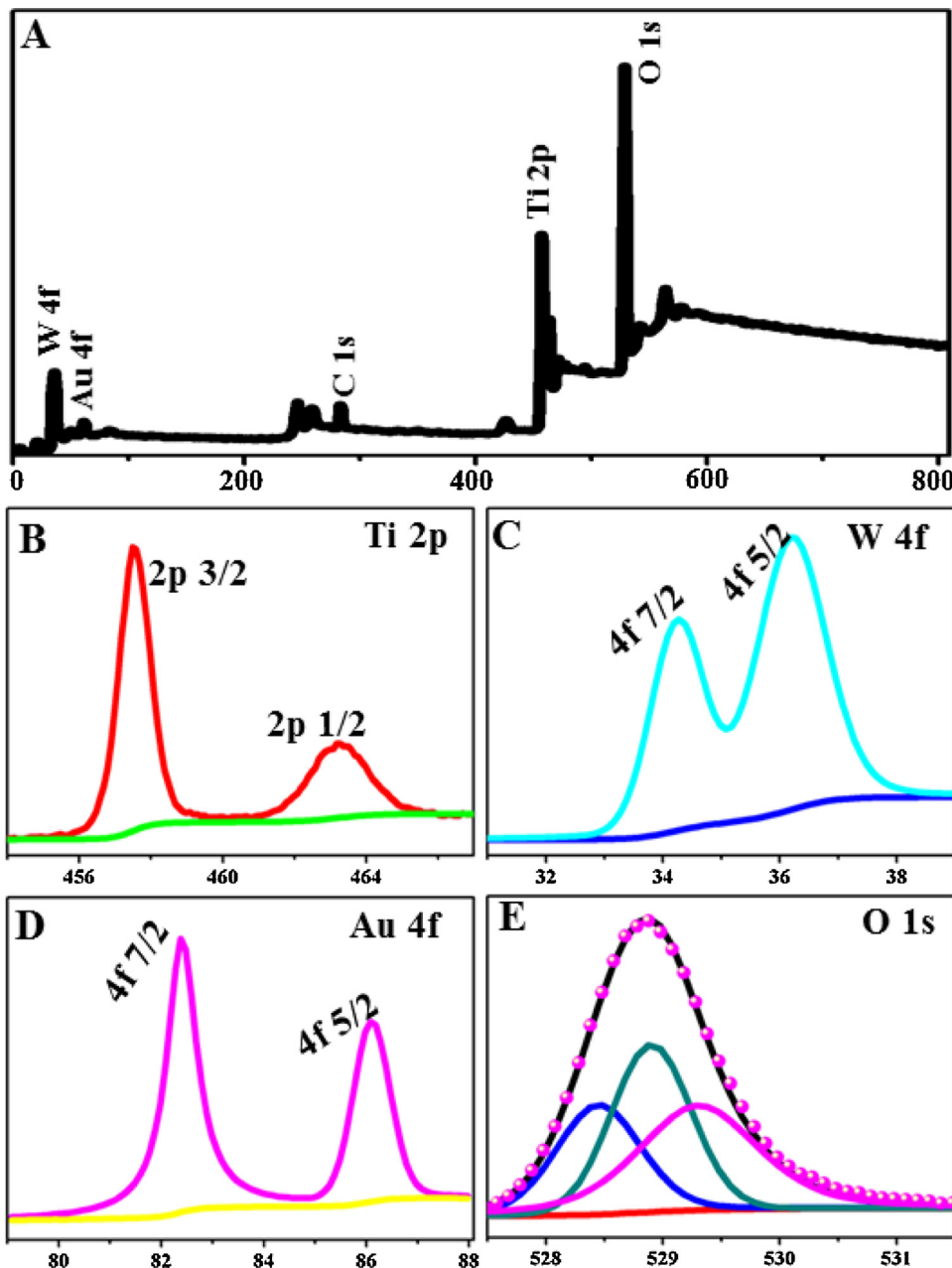


**Fig. 5.** XPS spectra of the as-prepared S2 sample: (A) fully scanned spectra; (B) XPS spectra of Ti 2p; (C) XPS spectra of W 4f; (D) XPS spectra of Au 4f; (E) fitting spectra of O 1s.

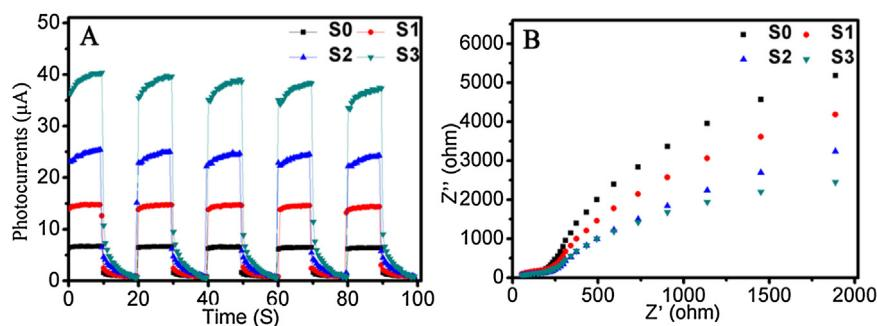


**Fig. 6.** Photocurrents (A) and EIS (B) of as-prepared samples.

$H_2$  production of pure  $TiO_2$  is almost undetectable, after being coupled with  $WO_3$ ,  $H_2$  production rate is increasing, reached

26.12  $\mu\text{mol}/\text{h}$ . Notably,  $H_2$  production of the ternary  $TiO_2/WO_3/Au$  composite nanofibers is significantly improved compared with

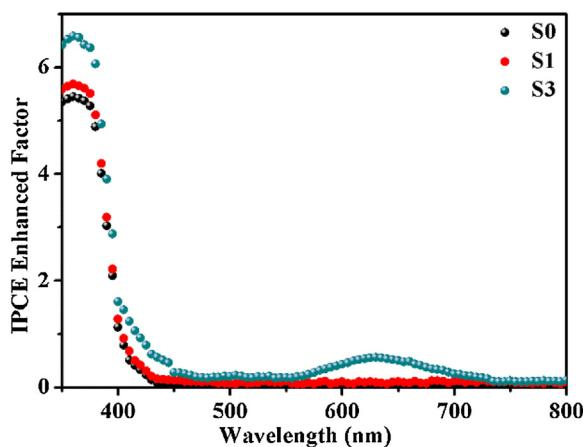
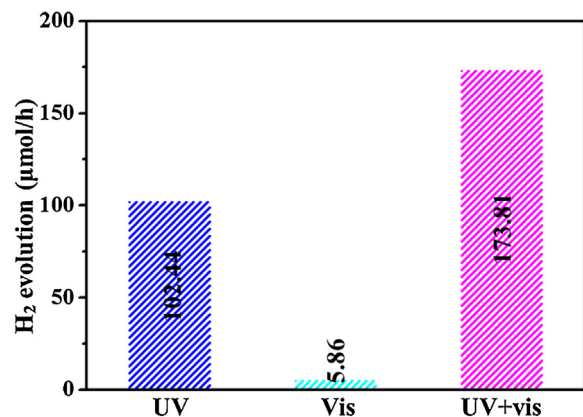


Fig. 7. IPCE spectrum of the as prepared samples.

$\text{TiO}_2$  nanofibers and  $\text{TiO}_2/\text{WO}_3$  nanofibers. And when the content of Au is within a certain range,  $\text{H}_2$ -production is higher when the content of Au is getting higher,  $\text{H}_2$  production rate of S2 and S3 is 182.93 and 269.63  $\mu\text{mol}/\text{h}$  respectively. As shown in Fig. 8(B, C), under the irradiation of UV+vis and UV light respectively, no obviously loss of photocatalytic performance was observed for S3 being used for 4 cycles. It was indicated that the  $\text{TiO}_2/\text{WO}_3/\text{Au}$  composite nanofibers displayed an efficient photoactivity and could be easily recycled. Fig. 8D shown the difference of  $\text{H}_2$  production rate of S3 under UV+vis and UV light, compared with the  $\text{H}_2$  production rate under the irradiation of UV light, the  $\text{H}_2$  production rate of S3 under the irradiation of UV+vis was increased 62.8%, this enhancement (EM) may be attributed to the SPR effect of Au. In order to better verify the synergistic effect of Schottky and SPR effect of Au, we also tested the photocatalyst hydrogen production activity of S3 sample under Vis light irradiation, as is shown in Fig. S2, the hydrogen production activity of S3 sample is 165.57  $\mu\text{mol}/\text{h}$ , 75.64  $\mu\text{mol}/\text{h}$  and 269.63  $\mu\text{mol}/\text{h}$  under UV, Vis and UV+Vis light irradiation, respectively. The hydrogen production activity of S3

Fig. 9. Hydrogen production rate of Au/TiO<sub>2</sub> nanofibers under different light irradiation.

sample under UV+Vis light irradiation is higher than the sum of the hydrogen production activity of S3 sample under UV and Vis light irradiation. Which may be attributed to the synergistic effect of SPR and Schottky effect of Au. We have revised and made a mark in the manuscript. Moreover, in order to better illustrate the synergies of SPR and Schottky effect of Au, we prepared S3 sample without the addition of  $\text{WO}_3$ , and studied its photocatalytic performance, the hydrogen production rate is shown in Fig. 9. From the figure we can see that the hydrogen production rate of Au/TiO<sub>2</sub> nanofibers under UV, Vis and UV+vis is 102.44  $\mu\text{mol}/\text{h}$ , 5.68  $\mu\text{mol}/\text{h}$  and 173.81  $\mu\text{mol}/\text{h}$ , respectively. The hydrogen production rate of Au/TiO<sub>2</sub> nanofibers under Vis irradiation is very low and almost undetectable, but the hydrogen production rate under UV+vis irradiation is much higher than the hydrogen production rate under UV irradiation. This also confirms our statement on  $\text{TiO}_2/\text{WO}_3/\text{Au}$  nanofibers that the synergies of SPR and Schottky effect of Au promoting the hydrogen production.

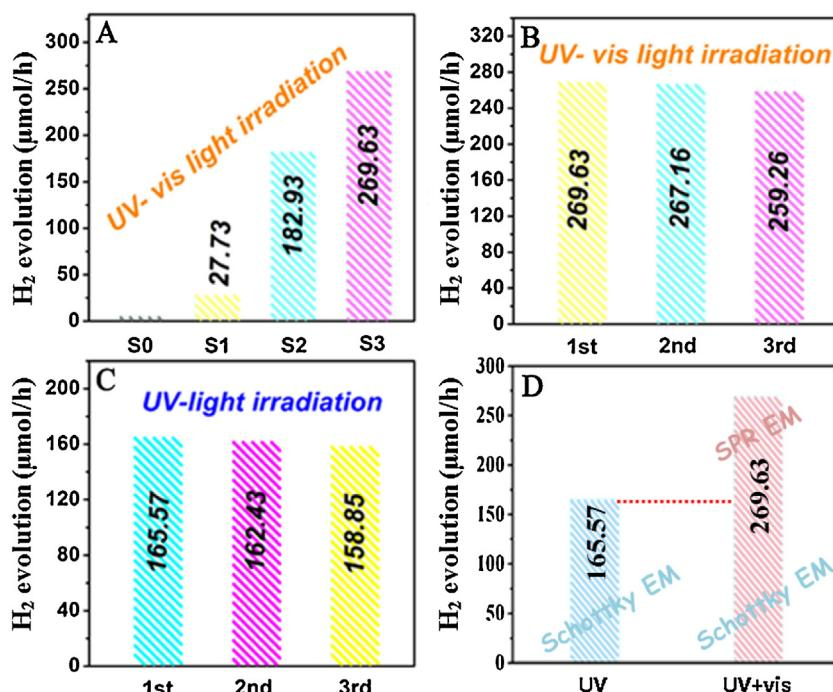
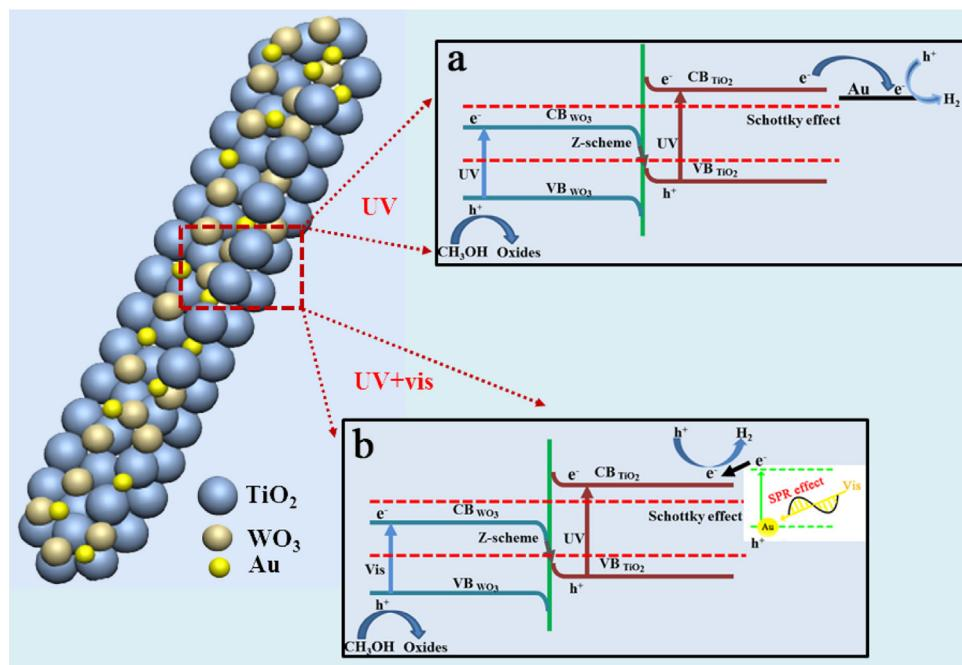


Fig. 8. Photocatalytic hydrogen production activity.



**Fig. 10.** Schematic diagram of the photocatalytic H<sub>2</sub> generation over the ternary TiO<sub>2</sub>/WO<sub>3</sub>/Au composite nanofibers.

### 3.8. Postulated photocatalytic mechanism

In order to study the reason of the enhanced activities of the as-prepared ternary Z-scheme TiO<sub>2</sub>/WO<sub>3</sub>/Au heterostructures composite nanofibers, an energy level diagram showing the positions of the bands of TiO<sub>2</sub>, WO<sub>3</sub> and Au is presented in Fig. 10. As shown in Fig. 10a, the CB of WO<sub>3</sub> is between the CB and VB of TiO<sub>2</sub>, and the VB of WO<sub>3</sub> is lower than the VB of TiO<sub>2</sub>, so it can form band bending and artificial Z-scheme when WO<sub>3</sub> contact with TiO<sub>2</sub>. Under the irradiation of UV light, the photogenerated electrons of WO<sub>3</sub> transferred to the VB of TiO<sub>2</sub>, and recombination with the hole of TiO<sub>2</sub>, promoting an effective charge separation. Besides, the photogenerated electrons of TiO<sub>2</sub> transferred from the CB of TiO<sub>2</sub> to Au nanoparticles, further promoted the charge separation. In this system, Au as an electron collector and WO<sub>3</sub> as a hole collector, thus promoting charge separation. As shown in Fig. 10b, under the irradiation of UV + vis light, the hot plasmonic electrons of Au can be transformed to the CB of TiO<sub>2</sub>, thus improving H<sub>2</sub> production rate. There are two major role Au nanoparticles played in this Au/TiO<sub>2</sub>/WO<sub>3</sub> heterojunction photocatalyst system. The first one is to transfer electron from the TiO<sub>2</sub> surface to react with H<sup>+</sup> in water for hydrogen production. Another positive effect is that photoexcited electrons of gold surface plasmon may be injected into the TiO<sub>2</sub> conduction band, creating separated electrons and holes. Therefore, this may not only improve the visible light absorption but also reduce the chance of recombination of photoinduced electron-hole pairs, hence increasing the photocatalytic hydrogen production activity.

In summary, we have successfully realized multichannel improvement of charge-carrier based on the ternary Z-scheme TiO<sub>2</sub>/WO<sub>3</sub>/Au heterostructures composite nanofibers by electro-spinning technique. The H<sub>2</sub> production rate of the as-prepared composite materials was greatly enhanced comparing with the pure TiO<sub>2</sub> nanofibers and TiO<sub>2</sub>/WO<sub>3</sub> nanofibers. The enhanced activities were mainly attributed to the Schottky effect and Z-scheme photosynthetic heterojunction system, WO<sub>3</sub> as a hole collector and Au as an electron collector, promoting effective charge separation. More importantly, SPR effect of Au further promoted charge separation and absorption of visible light. On the basis of the

Z-scheme photosynthetic heterojunction system, the synergistic effect of Schottky and SPR effect further improve the performance of photocatalytic H<sub>2</sub> production. Notably, the free-standing 3D nanotubes network structure could improve photocatalyst's performance of separation. And, it is expected that the nanofibers network will promote their industrial application as clean energy materials.

### Acknowledgments

The present work is supported financially by the National Natural Science Foundation of China (Nos. 51502269, 51001091, 111174256, 91233101) and Outstanding Young Talent Research Fund of Zhengzhou University (No. 1521320023).

### Appendix A. Supplementary data

Supplementary data associated with this article can be found, in the online version, at <http://dx.doi.org/10.1016/j.apcatb.2017.03.050>.

### References

- [1] A. Fujishima, K. Honda, *Nature* 238 (1972) 37–38.
- [2] J. Yan, G. Wu, N. Guan, L. Li, *Appl. Catal. B: Environ.* 152 (2014) 280–288.
- [3] Y. Ma, X. Wang, Y. Jia, X. Chen, H. Han, C. Li, *Chem. Rev.* 114 (2014) 9987–10043.
- [4] J. Yu, L. Qi, M. Jaroniec, *J. Phys. Chem. C* 114 (2010) 13118–13125.
- [5] A. Linsebigler, G. Lu, J.T. Yates, *Chem. Rev.* 95 (1995) 735–758.
- [6] L. Yu, D. Wang, D. Ye, *Sep. Purif. Technol.* 156 (2015) 708–714.
- [7] Z. Zhang, C. Shao, X. Li, L. Zhang, H. Xue, C. Wang, Y. Liu, *J. Phys. Chem. C* 114 (2010) 7920–7925.
- [8] T. Cao, Y. Li, C. Wang, Z. Zhang, M. Zhang, C. Shao, Y. Liu, *J. Mater. Chem.* 21 (2011) 6922–6927.
- [9] P. Zhang, C. Shao, M. Zhang, Z. Guo, J. Mu, Z. Zhang, X. Zhang, Y. Liu, *J. Hazard. Mater.* 217 (2012) 422–428.
- [10] J. Jin, J. Yu, D. Guo, C. Cui, W. Ho, *Small* 11 (2015) 5262–5271.
- [11] C. Liu, J. Tang, H.M. Chen, B. Liu, P. Yang, *Nano Lett.* 13 (2013) 2989–2992.
- [12] J. Yan, H. Wu, H. Chen, Y. Zhang, S.F. Liu, *Appl. Catal. B: Environ.* 191 (2016) 130–137.
- [13] W. Yu, D. Xu, T. Peng, *J. Mater. Chem. A* 3 (2015) 19936–19947.
- [14] J. Hu, L. Wang, P. Zhang, C. Liang, G. Shao, *J. Power Sources* 328 (2016) 28–36.
- [15] S. Kamimura, T. Miyazaki, M. Zhang, Y. Li, T. Tsubota, T. Ohno, *Appl. Catal. B: Environ.* 180 (2016) 255–262.

[16] J. Jiao, Y. Wei, Z. Zhao, W. Zhong, J. Liu, J. Li, A. Duan, G. Jiang, *Catal. Today* 258 (2015) 319–326.

[17] N.T. Nguyen, J. Yoo, M. Altomare, P. Sschmuki, *Chem. Commun.* 50 (2014) 9653–9656.

[18] Y. Ide, M. Matsuoka, M. Ogawa, *J. Am. Chem. Soc.* 132 (2010) 16762–16764.

[19] M. Murdoch, G.I. Waterhouse, M.A. Nadeem, J.B. Metson, M.A. Keane, R.F. Howe, J. Llorca, H. Idriss, *Nature. Chem.* 3 (2011) 489–492.

[20] P. Zhang, C. Shao, X. Li, M. Zhang, X. Zhang, Y. Sun, Y. Liu, *J. Hazard. Mater.* 237 (2012) 331–338.

[21] B. Wu, D. Liu, S. Mubeen, T.T. Chuong, M. Moskovits, G.D. Stucky, *J. Am. Chem. Soc.* 138 (2016) 1114–1117.

[22] C. Liu, D. Yang, Y. Jiao, Y. Tian, Y. Wang, Z. Jiang, *ACS Appl. Mater. Interfaces* 5 (2013) 3824–3832.

[23] P. Zhang, L. Wang, X. Zhang, C. Shao, J. Hu, G. Shao, *Appl. Catal. B: Environ.* 166 (2015) 193–201.

[24] X. Zhang, P. Zhang, L. Wang, H. Gao, J. Zhao, C. Liang, J. Hu, G. Shao, *Appl. Catal. B: Environ.* 192 (2016) 17–25.

[25] M. Zhang, C. Shao, Z. Guo, Z. Zhang, J. Mu, T. Cao, Y. Liu, *ACS Appl. Mater. Interfaces* 3 (2011) 369–377.

[26] A.L. Linsebigler, G.Q. Lu, J.T. Yates Jr., *Chem. Rev.* 95 (1995) 735–758.

[27] E. Della Gaspera, M. Bersani, G. Mattei, T.L. Nguyen, P. Mulvaney, A. Martucci, *Nanoscale* 4 (2012) 5972–5979.

[28] P. Zhang, C. Shao, Z. Zhang, M. Zhang, J. Mu, Z. Guo, Y. Sun, Y. Liu, J. Mater. Chem. 21 (2011) 17746–17753.

[29] Q. Han, B. Wang, J. Gao, Z. Cheng, Y. Zhao, Z. Zhang, L. Qu, *ACS Nano* 10 (2016) 2745–2751.

[30] J. Liu, Y. Liu, N. Liu, Y. Han, X. Zhang, H. Huang, Y. Lifshitz, S. Lee, J. Zhong, Z. Kang, *Science* 347 (2015) 970–974.

[31] Z. Zhang, Y. Huang, K. Liu, L. Guo, Q. Yuan, B. Dong, *Adv. Mater.* 27 (2015) 5906–5914.

[32] J.E.B. Randles, *Discuss. Faraday Soc.* 1 (1947) 11–19.

[33] H. Zhao, M. Wu, J. Liu, Z. Deng, Y. Li, B.L. Su, *Appl. Catal. B: Environ.* 184 (2016) 182–190.

[34] J. Li, S.K. Cushing, P. Zheng, T. Senty, F. Meng, A.D. Bristow, A. Manivannan, N. Wu, *J. Am. Chem. Soc.* 136 (2014) 8384–8449.

[35] Z. Zhang, Z. Wang, S.W. Cao, C. Xue, *J. Phys. Chem. C* 117 (2013) 25939–25947.